Composite Structures 125 (2015) 202–211

Contents lists available at ScienceDirect

Composite Structures

journal homepage: www.elsevier.com/locate/compstruct

Ballistic performance of composite metal foams

Matias Garcia-Avila [a], Marc Portanova [b], Afsaneh Rabiei [a,*]

[a] Advanced Materials Research Lab, Department of Mechanical and Aerospace Engineering, North Carolina State University, Raleigh, USA
[b] Aviation Applied Technology Directorate (AATD), U.S. Army Research, Development & Engineering Center, Fort Eustis, USA

ARTICLE INFO

Article history:
Available online 29 January 2015

Keywords:
Composite metal foam
Dynamic loading
Hollow spheres
Powder metallurgy
Ballistics
Finite element analysis

ABSTRACT

The application of advance materials to manufacture hard armor systems has led to high performance ballistic protection. Due to its light-weight and high impact energy absorption capabilities, composite metal foams have shown good potential for applications as ballistic armor. A high-performance light-weight composite armor system has been manufactured using boron carbide ceramics as the strike face, composite metal foam processed by powder metallurgy technique as a bullet kinetic energy absorber interlayer, and aluminum 7075 or Kevlar™ panels as backplates with a total armor thickness less than 25 mm. The ballistic tolerance of this novel composite armor system has been evaluated against the 7.62 × 51 mm M80 and 7.62 × 63 mm M2 armor piercing projectiles according to U.S. National Institute of Justice (NIJ) standard 0101.06. The results showed that composite metal foams absorbed approximately 60–70% of the total kinetic energy of the projectile effectively and stopped both types of projectiles with less depth of penetration and backplate deformation than that specified in the NIJ 0101.06 standard guidelines. Finite element analysis was performed using Abaqus/Explicit to study the failure mechanisms and energy absorption of the armor system. The results showed close agreement between experimental and analytical results.

1. Introduction

High-performance hard armor systems for ballistic protection of aircraft, ground and amphibious vehicles, and personnel have always been the subject of study for researchers. Hard armor systems typically consists of multiple layers, with a ceramic or ceramic composite plate at the strike face, backed with a ductile material such as ballistic steel or aluminum, or a high performance fiber reinforced composite. This hybrid arrangement of layers allows the armor system to defeat the projectile upon impact, with the ceramic layer blunting and eroding the projectile due to its high hardness, and the more ductile/high tensile backing plate absorbing the residual kinetic energy of the fractured or deformed projectile through plastic deformation [1]. A variety of armor options are already available, however each one has its own limitations restricting their widespread use in many applications. The development of light-weight combat technology, such as aircraft and amphibious vehicles, and the need to improve higher mobility for ground troops requires the continuous reduction of armor weight while increasing their ballistic performance.

Composite armors made with ceramic strike face and high-strength fiber reinforced composites have been widely studied as light-weight armors in the past. Several types of ceramic materials, such as aluminum oxide (Al_2O_3), boron carbide (B_4C), silicon carbide (SiC), silicon nitride (Si_3N_4), and combinations of those are typically used as the strike face plate in armor systems [2–6]. These ceramics are combined with high-tensile strength back plates made of aramid fiber composites such as Kevlar™ and Twaron™, or polyethylene composites such as Spectra™ or Dyneema™ to absorb the kinetic energy of the projectile. Although some of these combinations perform to some extent, the high cost of the constituents along with their heavy weight leaves room for improvement.

Composite metal foam (CMF) is low-weight high-strength metal foam manufactured using hollow metallic spheres embedded in a solid metal matrix. This material has shown superior mechanical properties compared to any other metal foam [7–15]. These outstanding qualities of CMFs are further improved under high-speed impact type of loading (similar to that in ballistic impact) compared to quasi-static loading [16]. These properties have made composite metal foams strong candidates for applications in composite armor systems. In this paper, CMF manufactured with 2 mm steel hollow spheres, embedded in a stainless steel matrix, and processed using powder metallurgy technique, was used to fabricate a new light-weight high performance composite armor

* Corresponding author at: Department of Mechanical and Aerospace Engineering, North Carolina State University, 911 Oval Drive, Campus Box 7910, Raleigh, NC 27695, USA. Tel.: +1 919 513 2674; fax: +1 919 515 7968.
E-mail address: arabiei@ncsu.edu (A. Rabiei).

http://dx.doi.org/10.1016/j.compstruct.2015.01.031
0263-8223/

system. The CMF was bonded to a ceramic plate on the strike face. Some samples were tested without any backing plates and some used a thin layer of aluminum or Kevlar™ backplate behind the CMF. Ballistic testing was performed using U.S. National Institute of Justice (NIJ) standard 0101.06 [17] for 7.62 × 51 mm M80 (Type III) and 7.62 × 63 mm M2 Armor Piercing (AP) (Type IV) threats.

A finite element approach was used to simulate ballistic impact and predict the energy absorbed by the composite metal foam (CMF) layer within the composite armor system. A full 3D model of the composite armor was studied using a Lagrangian formulation in Abaqus/Explicit 16.3 commercial solver.

2. Material processing

Steel–steel composite metal foam (S–S CMF) panels were manufactured using hollow spheres embedded in a stainless steel powder matrix and processed using powder metallurgy technique previously developed [8,10,12,16,18]. Hollow steel spheres with 2 mm outer diameter and 200 μm sphere wall thickness were manufactured by Hollomet GmbH in Dresden, Germany using lost core technique [19,20]. 316L stainless steel powder with 44 μm particle size from North American Hoganas high Alloy LLC was used as matrix material. Fig. 1A shows a 30 × 30 cm CMF panel after processing.

Boron Carbide (B_4C) ceramic tiles were used as the strike plate, and Kevlar™ or aluminum 7075 panels were used as backing plates in the armor system. All plates were 30 × 30 cm with different thicknesses of ceramic or CMF to maintain a total thickness around 25 mm in all samples with or without backing plates.

The multi-layered composite armor system was assembled by bonding the CMF panel to a ceramic tile on one side, and either no backplate, or either an Al-7075 (Ceramic-CMF-AL) or a simple weave Kevlar™ plate with fiber ultimate strength of 2.9 GPa (Ceramic-CMF-KV) on the other side. The assembled sandwich panel was wrapped with a single layer of 6oz plain-weave fiber glass infused in epoxy and bonded using vacuum bagging techniques and room temperature curing, in an attempt to keep failed ceramic fragments from ejecting during impact. Fig. 1B shows the assembly of the composite armor system, with a backplate and a total thickness to about 25 mm. Table 1 shows some properties for each layer used in the composite armor plates, along with threat type and impact velocities.

3. Ballistic experiments

Ballistic testing of the composite armor system was performed using the guidelines included in the National Institute of Justice (NIJ) standard 0101.06 [17] for Type III (7.62 × 51 mm M80) and Type IV (7.62 × 63 mm M2 AP) threats. Fig. 2 shows a top view sketch of the setup for the ballistic experiments. The composite armor system was placed against a heated Roma Plastilina No. 1 (clay), following the standard guidelines, in order to monitor the

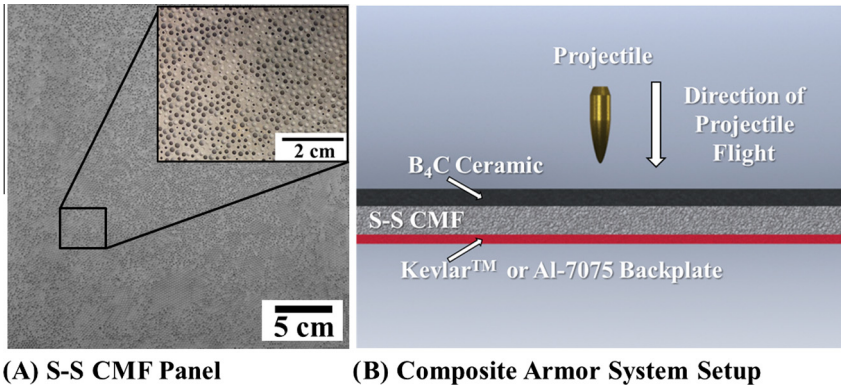

Fig. 1. (A) CMF panel processed using powder metallurgy technique for the application in armor system and (B) schematic of the side cross-section of the complete armor system showing CMF panel between a B_4C ceramic strike plate and a Kevlar™ or Al-7075 backplate (thicknesses not to scale).

Table 1
Some properties of composite armor plates, along with the threat types and impact velocities.

Armor thickness (cm)	Areal density (g/cm^2)	Threat	Backing plate	Mass bullet (g)	Impact velocity (m/s)
2.15	5.50	III	Aluminum	9.6	841.6
2.15	5.50	III	Aluminum	9.6	837.3
2.15	5.50	III	Aluminum	9.6	833.6
2.30	5.79	IV	Aluminum	10.8	863.2
2.30	5.79	IV	Aluminum	10.8	863.8
2.34	5.25	III	Kevlar	9.6	843.1
2.34	5.25	III	Kevlar	9.6	822.4
2.34	5.25	III	Kevlar	9.6	844.9
2.34	5.25	III	Kevlar	9.6	842.2
2.34	5.25	III	Kevlar	9.6	841.6
2.42	5.52	IV	Kevlar	10.8	892.1
2.45	5.50	IV	Kevlar	10.8	865.3
2.69	6.53	III	No backing	9.6	853.1
2.75	6.78	III	No backing	9.6	861.1
2.75	6.78	III	No backing	9.6	852.5
2.61	6.69	IV	No backing	10.8	869.0
2.69	6.69	IV	No backing	10.8	861.7

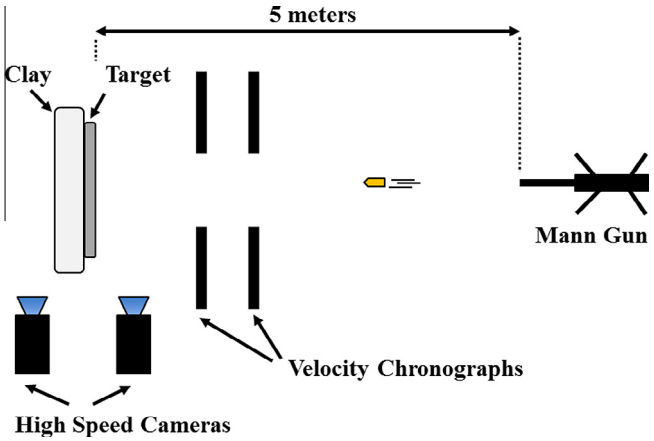

Fig. 2. Top view sketch of the ballistic test setup showing gun barrel, bullet velocity chronograph, target location, and high-speed cameras.

total out of plane deformation of the back of the armor, which is an indication of the potential body trauma caused by the impact. To prevent serious injury, NIJ 0101.06 specifies a maximum of 44 mm for the depth of penetration (DOP) into the clay and no limit on the diameter of the footprint, or back face signature (BFS). A "Mann" gun mounted on a two axis rig was used for the ballistic tests. Accurate measurements of the projectile speeds were possible using two velocity chronographs located between the gun and the target. Two high speed cameras were aimed at the impact face and the rear of the target to monitor the impacts. A 5 m distance was maintained between the gun and the target with a zero angle of obliquity the gun.

4. Finite element analysis

Studying the behavior of the armor system under ballistic impact using finite element analysis (FEA) provides an understanding of the failure mechanisms and a powerful and inexpensive tool for optimization of the ballistic system.

Hydrocodes are computer programs which handle propagation of shock waves, stress, strain, velocities, etc. within a continuum material as a function of time and position [21]. The relationship between these changes in the material state can be calculated using classical continuum mechanics such as conservation of mass, momentum, and energy. There are two major types of hydrocodes descriptions to create a system of differential equations, Lagrangian and Eulerian. To solve these equations, material properties are used to relate stress and strain and define failure mechanisms within the material, and equations of state relate internal energy and density changes with internal pressure [21]. Typically, Lagrangian solutions are simpler and require fewer equations to be solved than that of Eulerian definitions, thus requiring less computing power. For this reason, Lagrangian descriptions are preferred to solve the majority of finite element models.

4.1. Material models

Gordon Johnson and William Cook developed a constitutive model for ductile materials subject to high strain rates [22]. Their material model gives an expression of stress as a function of strain, strain rate, and temperature and has become the standard when modeling metals at high strain rates. Eq. (1) shows the expression of the Johnson–Cook material model, with σ being the stress, ε_p and $\dot{\varepsilon}^*$ the effective plastic strain and reference strain rate respectively, T^* the homologous temperature, and five material constants A, B, C, n, and m.

$$\sigma = [A + B\varepsilon_p^n][1 + C\ln\dot{\varepsilon}^*][1 - T^{*m}] \quad (1)$$

Constant A represents the yield strength, with B and n being strain hardening constants of the material which can be obtained through quasi-static loading tests. Constant C is the strain rate sensitivity of the material and it is found from high strain rate testing. T^* gives a material softening effect with increasing temperature and can also be found by varying the temperature of the sample while testing. Due to the accurate prediction of the material strength by this model, several materials models for metals have already been developed by Johnson and Cook [22].

The behavior of ceramic face plate and the bullet has already been studied by other researchers [23,24]. The purpose of this FEA analysis is to study the behavior and energy absorption of composite metal foams at high-speed impacts. As a result, the focus of this study is on the behavior of CMF with the assumption that the ceramic failure has already taken place and the bullet has already been blunted. Although this model does not include the complete behavior of the armor system, it can serve as a parametric tool to understand the behavior of the composite foam and the aluminum backing plate as a coupled system.

Composite metal foam (CMF) has unique material properties that are not easy to fit into any preexisting constitutive material model. Typical stress–strain curve under quasi-static compression for S–S CMF manufactured using 2 mm spheres and powder metallurgy technique is shown in Fig. 3. Similar to all metallic foams, steel–steel composite metal foam is characterized by an elastic region, followed by a yield and a plateau region. During the "plateau" region, the porosities continue collapsing under compression, until all porosities are collapsed and the material starts behaving like a solid material. In the case of composite metal foams the presence of a matrix between spheres causes a strain hardening effect during the period in which spheres are collapsing, which is seen as a tilted plateau in the stress–strain curve shown in Fig. 3. Further details about the typical stress–strain curves of CMFs under compression can be found elsewhere [7,9]. When loading S–S CMF under high strain conditions, the material exhibits an increase in yield strength due to the inertial effects and cushioning effect caused by the compression of the air trapped in the porosities [16,25,26]. This effect is observed in Fig. 3 by the dotted curve corresponding to the dynamic behavior of steel composite foams at a strain rate of 3277 1/s tested in a using Hopkinson Bar system. Further details related to that experiment and resulted data are presented elsewhere [25]. The strain rate sensitivity of composite foams and the improvement in their energy absorption capabilities (ΔE_{abs}) at high strain rates can be easily observed in this figure at strain levels up to 25–30% strain. At higher strain levels (above 25–30%) the strength of the material matches to that under quasi-static loading. In this case, the energy absorption of the material was estimated to be between 2–3 times higher than that of quasi-static loading conditions [25,26]. Although the strain rate in ballistic testing is

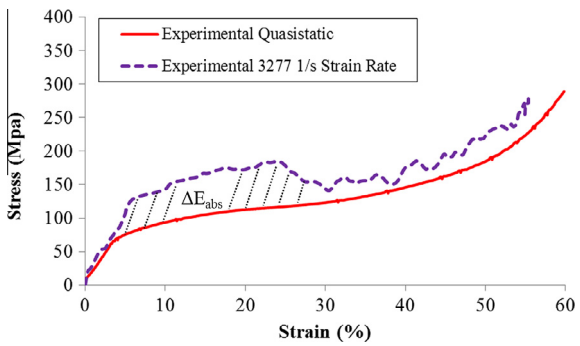

Fig. 3. Typical stress–strain curves for composite metal foam for quasi-static and dynamic loading curve [23].

much higher, defining the material property based on energy absorption is the only quantitative way to simulate the behavior of composite metal foams. This material definition provides a way to estimate the material energy absorption as a function of the actual compressive strain observed on the foam upon their inspection after ballistic impact. For these reasons, the stress–strain curve of CMFs under ballistic loading is predicted using the total value of the energy absorbed per unit volume of the compressed foam upon the inspection of the material after ballistic impact and considering the strengthening effect due to the strain rate sensitivity of CMFs.

4.2. Model setup

In first step single layer CMF and aluminum 7075-T6 panels with 300×300 mm dimensions were modeled separately and meshed in Abaqus/Explicit. Modeling the erosion of the projectile and the ceramic layers is considered beyond the scope of this study mainly because it is well established in the literature. As the result, our focus will be on the behavior of CMF layer with a backing plate. Since all of the experimental studies indicated that the ceramic layer spread the load onto the CMF layer leaving a perforation area of about 12 mm upon the impact of bullet, a solid and non-deformable cylinder with 12 mm diameter was used to simulate the effect of bullet- ceramic layer group and perforate the armor system similar to the experimental ballistic tests. Fig. 4 shows an illustration of the finite element model setup for a coarse mesh definition. Quadratic tetrahedral elements were used for all bodies and the model was constrained using a fixed support at the outside edges of the plates, as suggested in the literature [23,24,27–29]. The model setup shown in Fig. 4 corresponds to the coarse mesh definition, with large elements at the outside of the panel and a progressive finer mesh at the center of the panel. In order to obtain accurate results under bending, up to 3 elements were considered through the thickness of the aluminum layer in the coarser mesh definition. Smaller elements were considered for the finer mesh definition. Larger elements at the outside, where bending was not observed, should not affect the results at large.

The ballistic clay is considered to have a yield strength of 1 MPa with an elastic-perfectly plastic behavior. A pressure of 1 MPa was considered as a support boundary condition on the back of the aluminum plate to simulate the resistance provided by the clay during the ballistic tests. Frictionless contact definition was defined for all surfaces [27] and general contact definitions were considered between all elements, in agreement with the literature [23,27,28]. Lagrangian formulation was used to solve the conservation equations. The energy absorbed by each panel was obtained from the simulation and compared to the experimental tests.

4.3. Material model definitions

Due to the complexity of the composite armor system, several material constitutive models were considered for each layer material:

4.3.1. Aluminum 7075-T6 backing plate

A Johnson–Cook constitutive material model was considered for the aluminum backing plates used in the composite armor with the parameters [30] shown in Table 2.

4.3.2. Steel–steel composite metal foam

In order to maintain the shape of the stress–strain curve shown in Fig. 3 as a qualitative criterion under high-strain rate loading, a multi-linear stress–strain definition is used in the model to define the material response and shown in Fig. 5. Our previous studies indicated that the CMFs exhibit a strengthening effect due to the strain rate sensitivity of CMFs (Fig. 3) [25]. In this study, the energy absorbed per unit volume of CMF under ballistic impacts in experimental studies [26] is used to estimate the values of the yield and plateau strength. The density of the material is considered 2.8 g/cm^3, with an elastic modulus of 13.2 GPa and Poisson ratio of 0.1.

To minimize mesh size dependence of the FEA results, three different mesh sizes of coarse, medium, and fine were used to simulate penetration impact on an aluminum backing plate. Since the load would be applied at the center of the plate, a center area of

Table 2
Johnson–Cook and elastic material properties for Al7075-T6 plate.

Parameter	Al7075-T6[33]
Density (kg/m^3)	2800
E (GPa)	72
Poisson's ratio (ν)	0.33
Specific heat (J/kg °C)	848
A (MPa)	546
B (MPa)	678
n	0.71
C	0.024
m	1.56
$\dot{\varepsilon}^*$ (s^{-1})	1.0
$T^{melting}$ (°C)	650

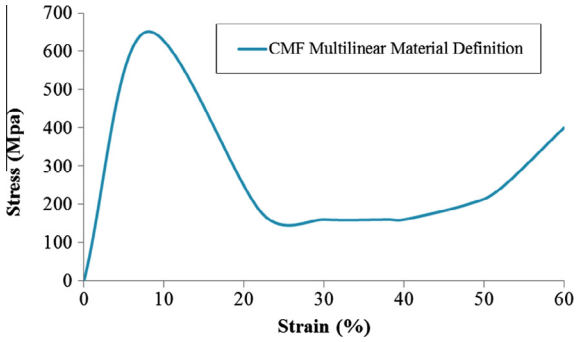

Fig. 5. Multi-linear stress–strain definition used for S–S CMF at ballistic relative strain rates.

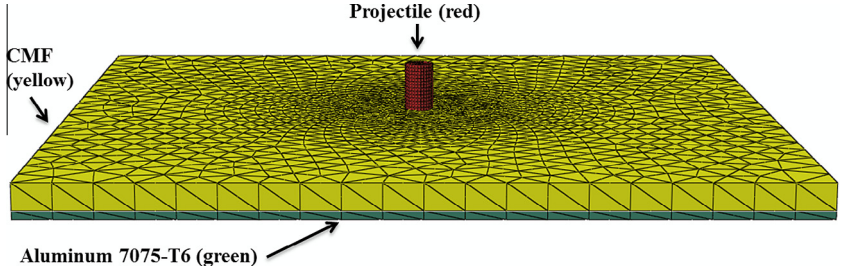

Fig. 4. Finite element model setup in Abaqus/Explicit 16.3 showing the mesh for the projectile (red), CMF layer (yellow) and Aluminum 7075-T6 backplate (green), thicknesses and dimensions are not in scale. (For interpretation of the references to color in this figure legend, the reader is referred to the web version of this article.)

the plate of 100 mm in diameter was meshed using smaller elements. For the coarse, medium, and fine meshes, the center area was meshed using 2, 0.9, and 0.7 mm maximum size elements and the outer area used 15, 10, and 9 mm maximum size elements respectively.

5. Results and discussion

5.1. Experimental results

All various types of samples without backplates and with Kevlar™ or Al backplates were able to stop the projectiles with DOPs less than 44 mm, which is considered the maximum allowable penetration according to the NIJ 0101.06 standard.

Digital images of the front strike face and rear face of a Ceramic-CMF (no backing) armor panel after NIJ-Type III impact test are shown in Fig. 6A-B respectively. The combination of ceramic and S–S CMF showed superior ballistic performance under Type III threats at impact speeds at or above NIJ standard requirements. The ceramic strike plate successfully blunted and eroded the projectiles upon impact. As seen in Fig. 6A a very small amount of NIJ-Type III bullet jacket material is left embedded in the armor.

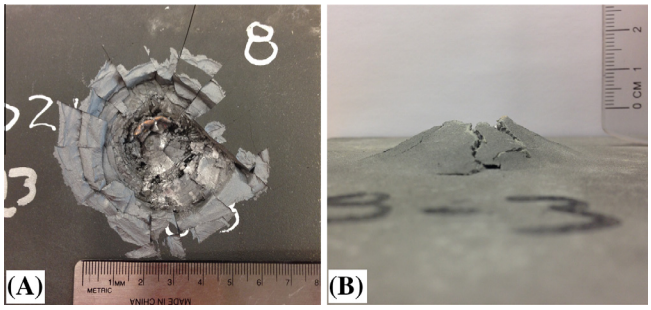

Fig. 6. Digital images of a Type III impact area on an armor system without backing plate: (A) front strike face showing complete arrest of the bullet and (B) rear face showing bulging of CMF and small amount of cracking due to tensile stresses.

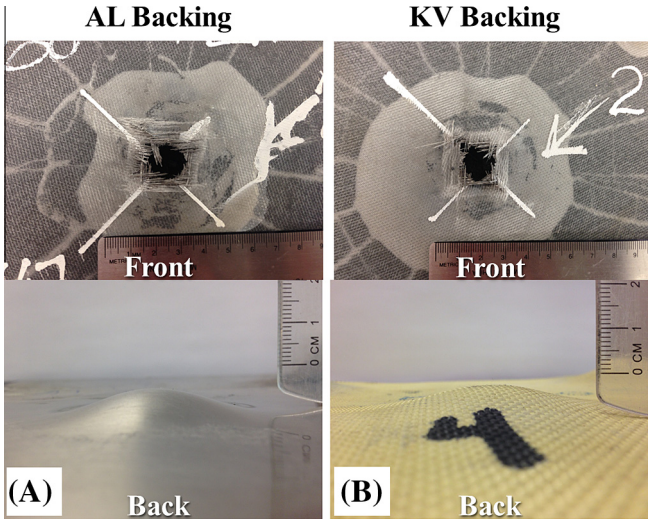

Fig. 7. Front-strike and rear face digital images of impact area of NIJ-Type III tests showing complete arrest of the bullet and rear bulging of backing plate for: (A) Ceramic-CMF-AL, (B) Ceramic-CMF-KV.

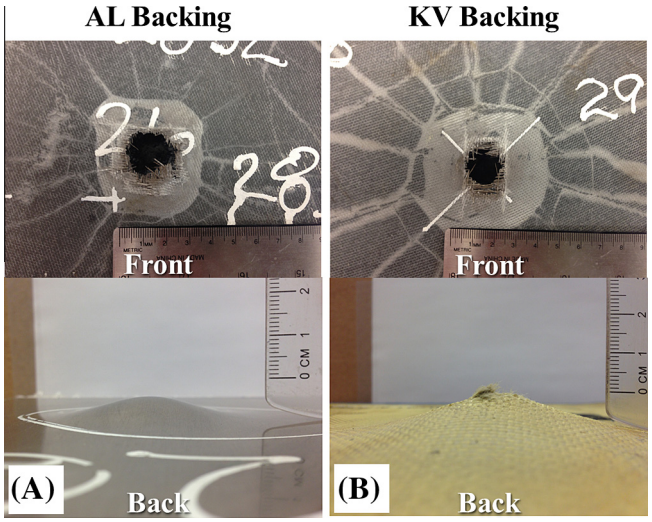

Fig. 9. Front-strike and rear face digital images of impact area of NIJ-Type IV tests showing complete arrest of the bullet and rear bulging of backing plate for: (A) Ceramic-CMF-AL, (B) Ceramic-CMF-KV.

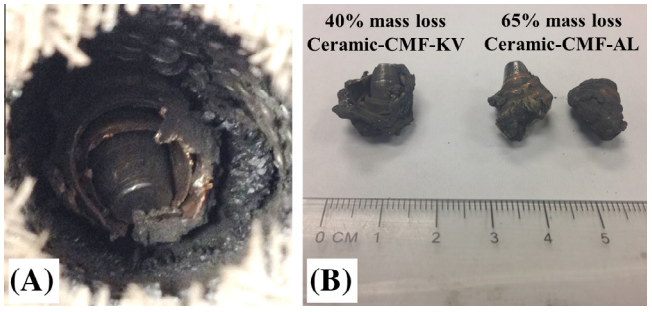

Fig. 10. (A) NIJ-Type IV AP projectile embedded in a Ceramic-CMF-KV sample after ballistic test at 865 m/s projectile speed and B) recovered AP projectiles from Ceramic-CMF-KV and Ceramic-CMF-AL showing 40–65% bullet mass loss.

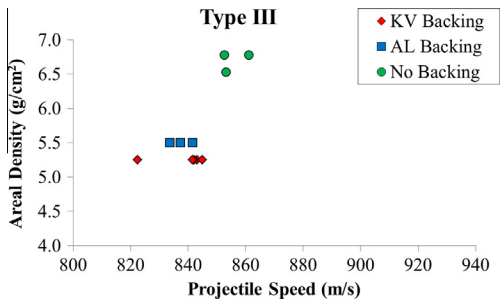

Fig. 8. Areal density for Ceramic-CMF, Ceramic-CMF-AL, and Ceramic-CMF-KV composite armor tested under Type III conditions at different impact speeds.

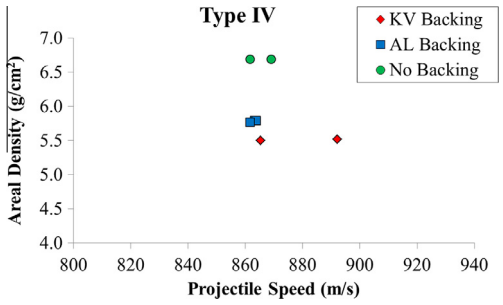

Fig. 11. Areal density for Ceramic-CMF, Ceramic-CMF-AL, and Ceramic-CMF-KV composite armor tested under Type IV conditions at different impact speeds.

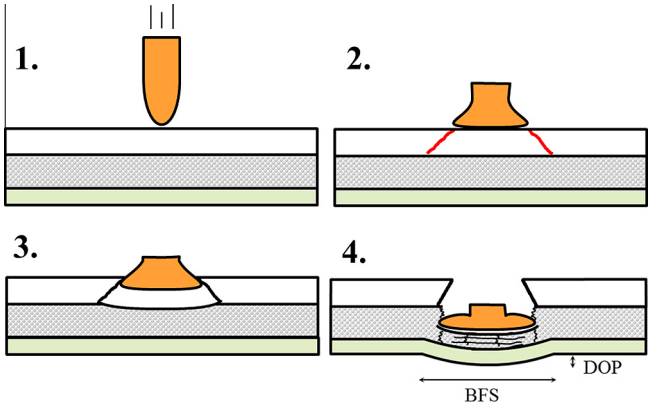

Fig. 12. Representation of the failure mechanism of Ceramic-CMF-Backing plate composite armor subjected to ballistic loading (thicknesses are not to scale).

Radial cracks on the ceramic plate are seen spreading out of the impact area, forming an outward crater seen in Fig. 6A. The ceramic layer successfully spread the load onto the CMF layer, which is going to absorb most of the kinetic energy of the bullet through plastic deformation and subsequent densification. As seen in Fig. 6B, this residual tensile stresses on the back of the CMF layer formed radial cracks extending from the impact area. Some fragments of the CMF were ejected from this area. This observation encouraged the idea of adding a thin layer of backplate behind the CMF to absorb those residual tensile stresses and catch any low velocity fragments.

Fig. 7A-B shows front and rear faces on Ceramic-CMF-AL and Ceramic-CMF-KV composite armor respectively after an NIJ-Type III impact. Both types of composite armor systems successfully stopped the projectiles for single and multi-hit scenarios, for bullet speeds at or higher than those specified by NIJ 0101.06 standard. It is observed that the ceramic plate caused failure of the projectile upon impact. A post impact inspection of the CMF layer showed that it had successfully absorbed the kinetic energy of the

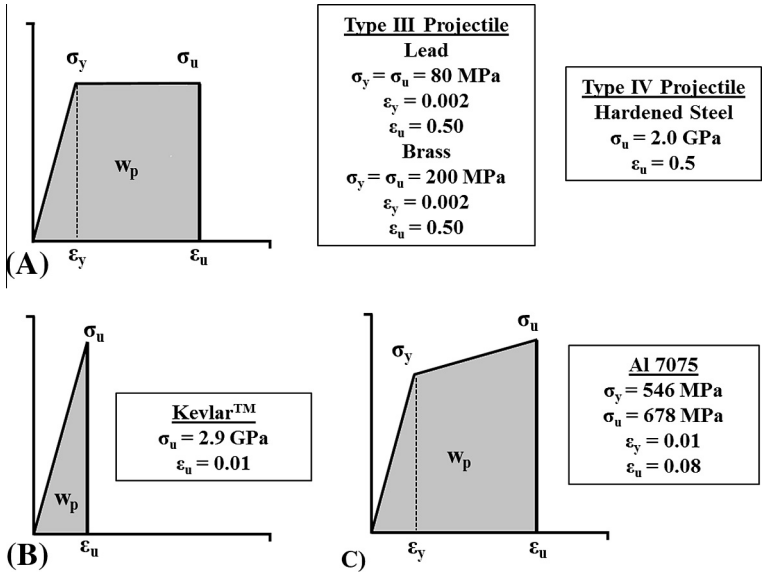

Fig. 13. Stress–strain curve used for analytical method to calculate plastic strain energy for each layer with (A) corresponding to hardened steel bullet core of NIJ-Type IV projectile and NIJ-Type III projectile, (B) Kevlar™ backing plate, and (C) aluminum 7075-T6 backing plate.

Table 3
Energy absorbed by each layer in the composite armor system as the % of bullet kinetic energy for both NIJ-Type III and Type IV impacts.

Threat type	Backing material	Impact velocity (m/s)	KE (J)	% E_{CMF}	% $E_{ceramic}$	% $E_{backing}$	% E_{bullet}	% E_{res}
III	Al	841.55	3399.41	57.98	7.58	17.94	13.65	0.01
III	Al	837.29	3365.03	63.03	7.87	10.13	13.79	0.01
III	Al	833.63	3335.69	60.14	7.06	13.68	13.91	0.01
III	kV	843.08	3411.74	70.73	11.90	3.75	13.60	0.02
III	kV	822.35	3246.05	64.15	17.62	3.91	14.29	0.03
III	kV	844.91	3426.55	70.13	13.53	2.77	13.54	0.03
III	kV	842.16	3404.34	61.95	15.83	8.53	13.63	0.06
III	kV	841.55	3399.41	63.57	16.88	5.85	13.65	0.05
III	None	853.15	3493.72	40.16	46.50	na	13.28	0.05
III	None	861.07	3558.92	23.53	63.39	na	13.04	0.04
III	None	852.54	3488.72	22.24	64.42	na	13.30	0.04
IV	Al	863.19	4023.56	56.19	8.46	18.66	19.86	0.01
IV	Al	863.80	4029.24	55.57	8.75	20.02	19.84	0.01
IV	Al	861.67	4009.36	53.76	8.39	30.17	19.93	0.02
IV	kV	892.15	4298.03	68.30	10.96	8.95	11.73	0.06
IV	kV	865.33	4043.47	66.00	14.13	7.36	12.47	0.04
IV	None	869.00	4077.83	47.13	22.71	na	30.15	0.01
IV	None	861.68	4009.46	40.43	28.90	na	30.67	0.01

projectile through compression and the aluminum and/or Kevlar™ backing plates supported the CMF layer as it was compressed, absorbing any residual tensile stresses and catching ejecta. Little or no fragments of projectile could be found after the NIJ-Type III tests on either one of the composite armor systems, which suggests a complete disintegration of the 7.62 × 51 M80 bullet for all samples tested.

Fig. 8 shows a comparison of the areal density for CMF (E_{CMF}) for Ceramic-CMF (no backing), Ceramic-CMF-AL, and Ceramic-CMF-KV samples for different impact velocities using NIJ-Type III projectiles. Using a stand-alone Ceramic-CMF composite armor system yielded successful results against Type III threats up to speeds at or above the NIJ standard requirements. A previous study by the authors suggested an increase on the yield strength of CMF material at high strain rates by over a factor of 2 at impact speeds up to 26 m/s [16]. In addition, a preliminary study of the ballistic properties of CMF suggested an energy absorption increase between 2–3 times higher at NIJ-Type III and IV impact speeds [26]. This increase in performance of CMF at high loading rates suggested a possible reduction in thickness of the ceramic and CMF layers, resulting in lighter and thinner armor plates. Also, adding Aluminum or Kevlar™ backing plates to the back of the CFM allowed a reduction of the thickness of both ceramic and CMF, which resulted in a weight reduction of 17% compared to the no backing samples.

Similarly, Fig. 9A-B shows front and rear faces of Ceramic-CMF-AL and Ceramic-CMF-KV composite armor respectively after impact of NIJ-Type IV projectiles. As can be seen, similar behavior of the armor system was obtained for Type IV projectiles. In this case, the partially disintegrated the hardened steel core and part of the bullet jacket were left embedded in the armor, as shown in Fig. 10A. The AP projectiles tested on the Ceramic-CMF-AL and Ceramic-CMF-KV showed 40–65% mass loss at impact velocities between 860–890 m/s (Fig. 10B), depending on the thickness of the ceramic.

Areal density for CMF (E_{CMF}) versus projectile speed for NIJ-Type IV tests are shown in Fig. 11 for Ceramic-CMF (no backing), Ceramic-CMF-AL, and Ceramic-CMF-KV composite armors. For

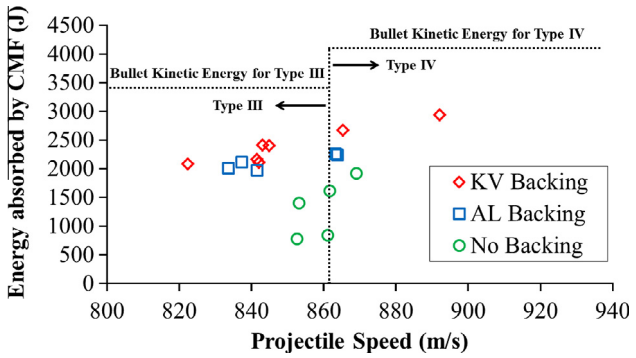

Fig. 14. Energy absorbed by CMF layer for both NIJ-Type III and Type IV tests in all composite armor systems tested.

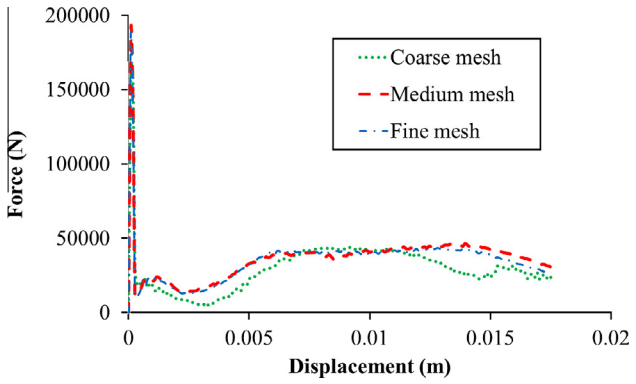

Fig. 15. Force–displacement results obtained for a 20 mm DOP simulation for the mesh sensitivity study for coarse, medium, and fine mesh definitions.

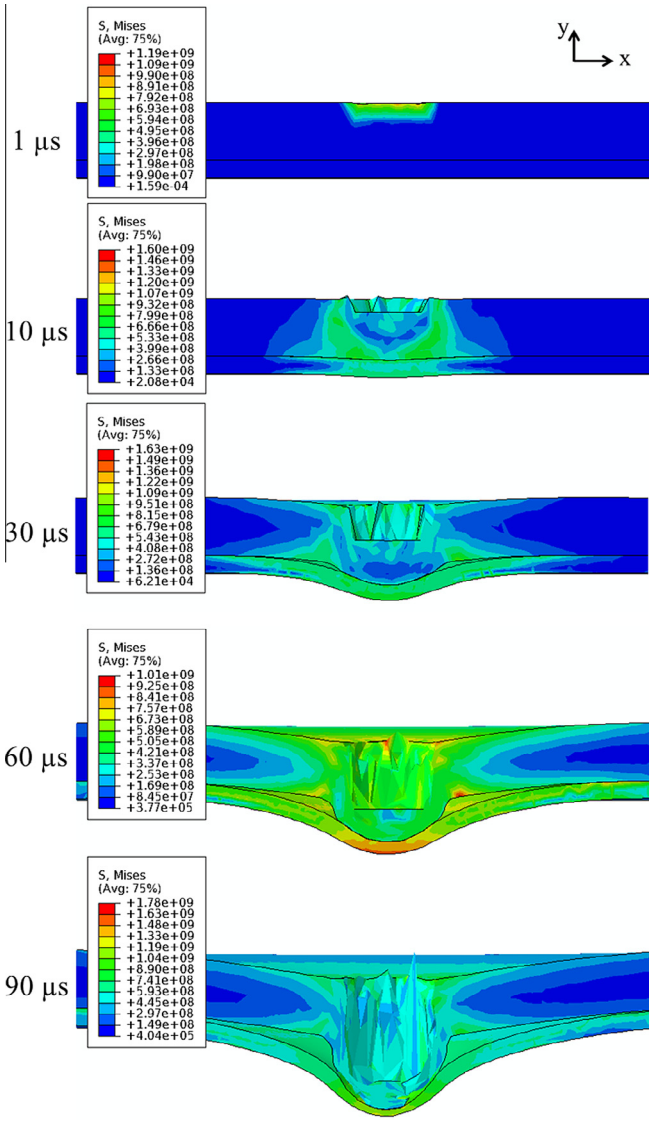

Fig. 16. Cross-sectional Von-Misses stress contour plots on CMF and Al layer obtained for a depth of penetration of 15.17 mm at 1, 10, 30, 60, and 90 µs.

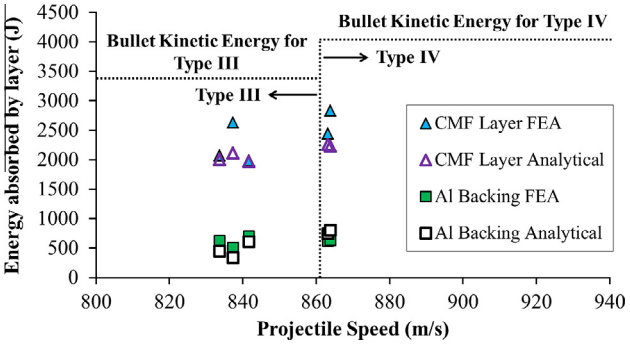

Fig. 17. FEA and analytical results for the energy absorbed by CMF and Al 7075-T6 layers for both NIJ-Type III and Type IV tests in all composite armor systems tested.

the Ceramic-CMF-AL, and Ceramic-CMF-KV composite armor systems designed for NIJ-Type IV threats, the addition of the backing plate and the reduction in thickness of ceramic and CMF layers resulted in a 13% and 20% weight reduction respectively compared to the Ceramic-CMF armor, with the Kevlar backed samples being 5% lighter than the AL backed samples due to a thinner ceramic layer used.

Fig. 12 illustrates the deformation mechanism of a Ceramic-CMF-backing plate composite armor system. As discussed before, upon impact, the hard ceramic plate blunts the projectile due to large compressive stresses developed at the projectile tip. When the compressive stresses travel through the ceramic layer and reach the interface between ceramic and CMF layer, tensile stresses are created due to the sudden change in mechanical impedance between the two layers. These tensile stressed are then reflected back towards the impact face. The intersection between the compressive and tensile stress waves traveling through the ceramic layer creates a high stress concentration area at angles between 25°–75° normal to the outer surface of the ceramic, which results in the failure of the ceramic material forming a Hertzian cone zone [31]. This cone detaches from the ceramic and serves to distribute the compressive load at the ceramic-CMF interface over a larger area. The residual tensile waves in the ceramic form circumferential and radial cracks and due to this localized fracture and comminution in the vicinity of the impact area, results in an outward crater at the impact face. As penetration progresses, compressive waves build up on the CMF layer until its yield point and further, deforming plastically at high compressive loads and absorbing the kinetic energy of the projectile. The light weight backing plate below the CMF layer absorbs any residual tensile stresses of the armor system, maintaining the integrity of the impact area and keeping debris contained inside the perforation. Using a combination of ceramic, CMF, and backing plate, provides a layer-based functional design solution where each constituent contributes in a collaborative fashion to the ballistic energy absorption process.

In ballistic impacts, most of the kinetic energy of the projectile is transformed into brittle fracture of the ceramic under compression and tension, plastic deformation of the projectile and backing plate, and heat. For this study, and since the local temperature at the point of impact could not be measured, the heat generation is considered negligible for energy calculations. Using an energy approach previously discussed [26], the energy absorbed by each component in the composite armor system can be approximated. Upon impact, the kinetic energy of the projectile (E_{KE}) is transferred to the armor system as the energy used for plastic deformation of the bullet (E_{bullet}), energy absorbed by the ceramic ($E_{ceramic}$), energy absorbed by CMF layer (E_{CMF}), energy absorbed by the backing plate ($E_{backing}$), and residual energy from clay deformation or debris ejected from the target in the event of complete penetration (E_{res},), as shown in Eq. (2):

$$E_{KE} = E_{bullet} + E_{ceramic} + E_{CMF} + E_{backing} + E_{res} \quad (2)$$

Similar studies on energy absorption of armor systems have been reported in the literature [32]. The energy per unit volume of material for the projectile, ceramic, backing plate, and clay can be calculated from their respective stress–strain curves by calculating the area under the curve using a strain energy (w_p) method according to Eq. (3)

$$w_p = \int \sigma d\varepsilon \quad (3)$$

where w_p is essentially the area under the stress–strain curve in J/m^3. Using material properties of each layer and multiplying the value of this strain energy by the total amount of material under deformation per layer (bullet, ceramic, backing plate, clay), the total kinetic energy dispersed by each component of the composite armor system is calculated. Fig. 13A-C shows a representation of each method of calculating strain energy for each layer of the composite armor against both NIJ-Type III and Type IV projectiles, where σ_y and ε_y are the yield strength of the material and the

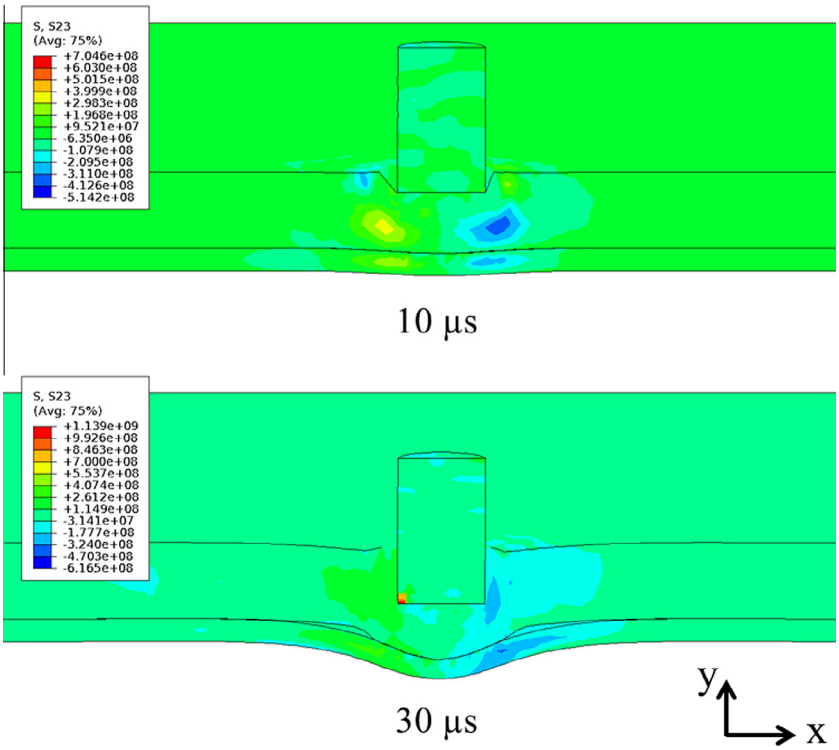

Fig. 18. Cross-sectional *x–y* shear plots for a 15.17 depth of penetration simulation, showing high shear areas on the CMF and aluminum layers.

corresponding strain (for ductile materials), σ_u and ε_u are the ultimate strength and corresponding ultimate strain, respectively. Properties of each component are obtained from the literature [22,30,33] and shown in Fig. 13.

Residual energy (E_{res}) was calculated from BFS and DOP measurements on clay, a σ_y of 1 MPa, along with the method shown in Fig. 13B, and residual velocities of particles obtained from high speed video.

Solving for E_{CMF} in Eq. (2) and substituting all energy values calculated gives the estimated energy absorption by the CMF layer. Values for all energy absorbed per layer in percentage of total kinetic energy are shown in Table 3.

Fig. 14 shows the kinetic energy absorbed by the CMF layer in the composite armor system for both NIJ-Type III and Type IV tests. As can be seen, with the appropriate arrangement of layers, CMF was capable of absorbing 60–70% of the kinetic energy of the bullet, proving the superior energy absorption capabilities of composite metal foams at high impact speeds. It is also observed that by adding a soft backing plate behind CMF, the areal density was decreased with no adverse effect on the energy absorption capabilities of the total composite armor system.

5.2. Finite element analysis results

5.2.1. Mesh sensitivity study

The penetrator's net nodal force reactions were obtained and plotted against projectile displacement for a depth of penetration of 20 mm (such DOP is selected based on our ballistic studies) (Fig. 15). No issues were encountered with over skewed elements for the 2 finer mesh definitions. It can be seen that the solution for both medium and fine meshes is comparable and a finer mesh does not provide a more accurate solution. For this reason, and to save on computing power, a medium mesh definition was used in the model.

Von-Mises stress plots for a 15.17 mm depth of penetration simulation are shown in Fig. 16 at 10, 30, 60, and 90 μs of penetration time. Compression of the CMF layer at 90 μs shows full densification up to 80% strain, with similar deformation pattern obtained in experimental tests. The aluminum backplate supports the rear face of the CMF, and deforms in tension absorbing the residual kinetic energy of the penetrator, leaving a bulging profile on the armor system similar to that shown in Fig. 7A and Fig. 9A.

Fig. 17 shows the simulation results for energy absorbed by CMF and aluminum layers for both Type III and Type IV bullet speeds compared to the experimental results. As can be seen, a close prediction of the energy dissipated by the aluminum plate is obtained for all tests. For the CMF layer, an over-prediction of the energy absorbed by the FEA model is seen in Fig. 17. Fig. 18 shows the high x-y shear stresses developed in the CMF layer under puncture by the penetrator. These shear stresses could cause failure in the material and could hinder plastic flow under ballistic loading, artificially raising the energy absorption of the material in the FEA model. However, behavior of CMF under shear loading has not been studied extensively and as the result it was not taken into account in this material model. Although close prediction of the behavior of CMF has been obtained by this model, further characterization of CMF under shear loading is needed to consider complete material failure definitions and develop a more accurate model.

6. Conclusions

Composite metal foam panels manufactured using 2 mm steel hollow spheres embedded in a stainless steel matrix and processed through powder metallurgy technique were used together with boron carbide ceramic and aluminum 7075 or Kevlar™ back panels to fabricate a new composite armor system. This composite armor was tested against NIJ-Type III and Type IV threats using NIJ 0101.06 ballistic test standard. The highly functional layer-based design allowed the composite metal foam to absorb the ballistic kinetic energy effectively, where the CMF layer accounted for 60–70% of the total energy absorbed by the armor system, and allowed the composite armor system to show superior ballistic performance for both Type III and IV threats.

Finite element analysis results for ballistic loading of the armor system closely predicted the behavior and energy absorption of the CMF and aluminum layers. The Kevlar system was not considered in the simulation since the results for the energy absorbed by CMF in the system with the aluminum layer were successful. However, the failure mechanisms of CMF under ballistic loading are complex and further characterization of the material under shear loading is necessary prior to establish a comprehensive model of its behavior under ballistic loading.

Acknowledgments

The authors would like to acknowledge North Carolina State University's Chancellor Innovation Fund (CIF) for its financial support that made this project possible. Special thanks to Dr. Robert Bryant and his team at the Advanced Materials and Processing Branch at NASA Langley Research Center, for granting access to their material processing facilities.

References

[1] Hetherington J, Smith P. Blast and Ballistic Loading of Structures. Oxford; Boston: CRC Press; 1994.
[2] Medvedovski E. Ballistic performance of armour ceramics: Influence of design and structure. Part 1. Ceram Int 2010;36:2103–15.
[3] Medvedovski E. Ballistic performance of armour ceramics: Influence of design and structure. Part 2. Ceram Int 2010;36:2117–27.
[4] David NV, Zheng JQ, Gao X-L. Ballistic resistant body armor: contemporary and prospective materials and related protection mechanisms. Appl Mech Rev 2009;62. 050802–050802.
[5] Tasdemirci A, Tunusoglu G, Güden M. The effect of the interlayer on the ballistic performance of ceramic/composite armors: experimental and numerical study. Int J Impact Eng 2012;44:1–9.
[6] Medvedovski E. Lightweight ceramic composite armour system. Adv Appl Ceram 2006;105:241–5.
[7] Rabiei A, O'Neill AT. A study on processing of a composite metal foam via casting. Mater Sci Eng A 2005;404:159–64. http://dx.doi.org/10.1016/j.msea.2005.05.089.
[8] Neville BP, Rabiei A. Composite metal foams processed through powder metallurgy. Mater Des 2008;29:388–96.
[9] Vendra LJ, Rabiei A. A study on aluminum–steel composite metal foam processed by casting. Mater Sci Eng A 2007;465:59–67.
[10] Rabiei A, Vendra LJ. A comparison of composite metal foam's properties and other comparable metal foams. Mater Lett 2009;63:533–6.
[11] Vendra L, Rabiei A. Evaluation of modulus of elasticity of composite metal foams by experimental and numerical techniques. Mater Sci Eng A 2010;527:1784–90.
[12] Rabiei A, Neville B, Reese N, Vendra L. New composite metal foams under compressive cyclic loadings. Mater Sci Forum 2007;539–543:1868–73.
[13] Vendra L, Neville B, Rabiei A. Fatigue in aluminum–steel and steel–steel composite foams. Mater Sci Eng A 2009;517:146–53.
[14] Vendra LJ, Brown JA, Rabiei A. Effect of processing parameters on the microstructure and mechanical properties of Al–steel composite foam. J Mater Sci 2011;46:4574–81.
[15] Brown JA, Vendra LJ, Rabiei A. Bending properties of al-steel and steel–steel composite metal foams. Metall Mater Trans A 2010;41:2784–93.
[16] Rabiei A, Garcia-Avila M. Effect of various parameters on properties of composite steel foams under variety of loading rates. Mater Sci Eng A 2013;564:539–47.
[17] NIJ 0101.06-U.S. Department of Justice. Ballistic Resistance of Body Armor NIJ Standard 0101.06 2008.
[18] Rabiei A, Vendra L, Reese N, Young N, Neville BP. Processing and characterization of a new composite metal foam. Mater Trans 2006;47:2148–53.
[19] Andersen O, Waag U, Schneider L, Stephani G, Kieback B. Novel Metallic Hollow Sphere Structures. Adv Eng Mater 2000;2:192–5.
[20] Stephani G, Kupp D, Claar TD, Waag U. Fabrication of Ti-based components with controlled porosity. Int Conf Powder Metall Part Mater 2001:50–8.

[21] Anderson Jr CE. An overview of the theory of hydrocodes. Int J Impact Eng 1987;5:33–59.
[22] Johnson GR, Cook WH. A constitutive model and data for metals subjected to large strains, high strain rates and high temperatures. In: Proc 7th Int Symp Ballist 1983; 21: p. 541–7.
[23] Bürger D. Rocha de Faria A, de Almeida SFM, de Melo FCL, Donadon MV. Ballistic impact simulation of an armour-piercing projectile on hybrid ceramic/fiber reinforced composite armours. Int J Impact Eng 2012;43:63–77.
[24] Feli S, Asgari MR. Finite element simulation of ceramic/composite armor under ballistic impact. Compos Part B Eng 2011;42:771–80.
[25] Rabiei A. Material with Improved Absorption of Collision Forces for Railroad Cars. Safety IDEA Project 20 final report, National Academy of Science 2014.
[26] Garcia-Avila M, Portanova M, Rabiei A. Ballistic performance of a composite metal foam-ceramic armor system. In: Proc metfoam 2013 2013.
[27] Iqbal MA, Chakrabarti A, Beniwal S, Gupta NK. 3D numerical simulations of sharp nosed projectile impact on ductile targets. Int J Impact Eng 2010;37:185–95.
[28] Vanichayangkuranont T, Maneeratan K, Chollacoop N. Numerical simulation of level 3A ballistic impact on ceramic/steel armor. In: The 20th conference of mechanical engineering network of thailand 2006.
[29] Teng X, Wierzbicki T, Huang M. Ballistic resistance of double-layered armor plates. Twenty-fifth anniv celebr issue honouring profr Norman Jones his 70th birthd 2008; 35: p. 870–84.
[30] Brar NS, Joshi VS, Harris BW. Constitutive model constants for Al7075-T651 and Al7075-T6. Am Inst Phys Conf Ser 2009;1195:945–8.
[31] Fountzoulas CG, LaSalvia JC. Improved modeling and simulation of the ballistic impact of tungsten-based penetrators on confined hot-pressed boron carbide targets. In: Swab JJ, Halbig M, Sanjaythur, editors. Adv. Ceram Armor VII. John Wiley & Sons, Inc.; 2012. p. 209–17.
[32] Naik NK, Kumar S, Ratnaveer D, Joshi M, Akella K. An energy-based model for ballistic impact analysis of ceramic-composite armors. Int J Damage Mech 2012. 1056789511435346.
[33] Peroni L, Scapin M. Mechanical properties at high strain-rate of lead core and brass jacket of a NATO 7.62 mm ball bullet 2012;26.